International Journal of Engineering Research-Online
A Peer Reviewed International Journal
ISSN: 2321-7758 http://www.ijoer.in editorijoer@gmail.com
Vol.14., Issue.3, 2026
July-Sept

RESEARCH ARTICLE

ISSN: 2321-7758

BaO-Mediated Grain Boundary Engineering in ZnO–MnO_2 Varistor Ceramics: Microstructure Evolution, Schottky Barrier Modulation, and Nonlinear Electrical Performance

Abbas Fadhal Shannoon
Geniuses High School for Outstanding Students, The General Directorate Al-Rusafa the Third, Ministry of Education, Baghdad-10059, Iraq
Email: knanybas71@gmail.com

DOI: 10.33329/ijoer.14.3.1

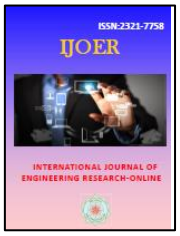

Article info
Article Received: 26/04/2026
Article Accepted: 09/06/2026
Published online: 14/06/2026

Abstract

ZnO-based varistors are widely used for surge protection; however, conventional Bi_2O_3-doped systems often degrade under DC electrical stress. This study investigates the influence of low-concentration BaO additions (0, 0.05, and 0.10 wt.%) on the structural, microstructural, optical, and electrical properties of ZnO–MnO_2 varistors. Ceramic composites were prepared by wet milling, uniaxial and cold-isostatic pressing, and pressureless sintering in air. X-ray diffraction confirmed the formation of a hexagonal wurtzite ZnO phase, while BaO incorporation induced slight lattice distortion and reduced crystallite size. Scanning electron microscopy revealed enhanced grain growth with increasing sintering temperature, whereas relative densities remained above 95%. Energy-dispersive spectroscopy indicated significant Ba segregation at grain boundaries. Optical measurements showed a reduction in bandgap energy from 3.34 to 2.79 eV after BaO addition. Electrical characterization demonstrated that the specimen containing 0.10 wt.% BaO and sintered at 1200 °C exhibited improved varistor performance, with a nonlinearity coefficient of 9 and a breakdown field of 140 V mm^{-1}, compared with values of 7 and 180 V mm^{-1} for the undoped composition. The enhanced electrical response is attributed to Ba-induced modification of grain boundaries and the formation of higher Schottky-type potential barriers. These results demonstrate that BaO is an effective grain-boundary engineering additive for optimizing low-voltage ZnO–MnO_2 varistors.

Keywords: ZnO varistors; BaO doping; Grain boundary engineering; Microstructure; Nonlinear electrical.

1. Introduction

Ceramic-based varistors based on ZnO demonstrate very strong nonlinear and non-ohmic I-V characteristics, making them very valuable for transient overvoltage suppression [1]. The reason for that is the relatively complex microstructure, which involves grains of the n-type ZnO semiconductor along with insulating and electronically conducting grain boundaries, forming a double Schottky barrier system [2]. Production of these ceramics involves powder metallurgy and the sintering technique. For example, approximately 98 mol% of ZnO is mixed with small quantities of such compounds as Bi_2O_3, Sb_2O_3, MnO_2, CoO, and Cr_2O_3 [3]. In the sintering procedure, Bi_2O_3 serves as a liquid phase, assisting in grain boundary formation [4]. Every component is involved in the specific task; for example, MnO_2, CoO, and Cr_2O_3 increase nonlinearity [5,6].

However, there are drawbacks to the conventional Bi_2O_3 varistors, such as electrical degradation under DC bias, which is due to oxygen-ion diffusion and modification of the Schottky barrier [7]. As such, extensive research has been conducted to develop new and alternative dopants to overcome this limitation. Transition metal oxides such as Mn, Ni, Zr, and Cr, along with rare-earth oxides Pr and Er, were found to offer better performance in terms of GB potential barriers and stability [8-14]. Flash, microwave, and two-step sintering have been used to modify the properties [15-17]. Table 1 lists representative studies on ZnO varistors. Whereas the behavior of various Bi_2O_3, V_2O_5, and Pr_6O_{11} systems is well studied in the literature, very little is known about the function of BaO as an important GB modifier in ZnO-MnO_2 ceramics. The ability of BaO to segregate at GBs, leading to secondary phases that act as a resistance source and contribute to varistor behavior, was shown in early papers [18]. However, despite numerous reports on the effects of the coupled low concentrations of BaO and MnO_2 doping, a common varistor material that has a great effect on the bulk chemistry and grain growth [19], there is not enough information about their interaction during sintering and the effects on the microstructure and properties of GB traps and barrier heights. Indeed, most recent literature focuses on the development of existing approaches using modifiers such as NiO and rare-earth elements, or on novel processing techniques [20–22]. In this case, the potential of BaO as an efficient and inexpensive GB modifier is underestimated. According to our best knowledge, no study considered 0.0-0.10 wt.% BaO additions to ZnO-MnO_2 varistors for temperatures 1050-1200 °C.

Table 1. Comparative summary of recent ZnO-based varistor studies

Reference	System/Dopant	Sintering Temp (°C)	Grain Size (μm)	α	Eb (V/mm)	Key Limitation
Feng et al. 2022 [11]	NiO–ZnO	1100	9–14	8–12	300–420	High breakdown field
Cui et al. 2023 [12]	Mn–ZnO (low-temp)	875–1000	5–10	15–20	80–120	Complex processing, low density
Tian et al. 2022 [13]	Cr_2O_3–ZnO	1150	8–15	10–18	250–400	Moderate nonlinearity
Zhang et al. 2021 [14]	Er_2O_3–ZnO	1150	10–20	12–22	200–350	High cost of rare earths

Liptai et al. 2024 [29]	Recycled ZnO	1100	10–20	8–12	300–500	Poor reproducibility
Hassan et al. 2025 [32]	Multi-dopant ZnO	1000–1200	10–25	8–15	200–380	Complexity of optimization
Present Study	BaO–ZnO–MnO_2	1200	42	9	140	Moderate α (improvement pathway identified)

Processing techniques are equally important. Flash sintering, spark plasma sintering, microwave sintering, and two-step or low-temperature sintering have been shown to greatly impact densification kinetics and defect chemistry [23–26]. Research on pre-calcination studies, sensitivity to cooling rates, and approaches to recyclability has been reported [27–29].

Altogether, this research shows that an integrated control strategy for doping, processing, and powder engineering is indispensable in developing high-performance ZnO varistors with improved electrical and thermal stability [30–32]. Thus, this study aims to systematically explore the effect of BaO doping at low concentrations (0, 0.05, 0.10 wt.% BaO) on the structural, microstructural, optical, and electrical properties of ZnO-MnO2 varistors, with emphasis on the sintering temperature window of 1050–1200°C. By analysing how the amount of BaO impacts the nonlinear behavior of ZnO-MnO2 varistors via its effect on the density, grain size, and phase distribution within the material, we will reveal BaO mechanism of action and its effect on GBs in ZnO-MnO2 varistors. It is hypothesized that BaO, which has a very strong segregation tendency into GBs owing to its large ionic radius, forms more effective GB barriers compared to traditional dopants at low concentrations.

2. Materials and Methods

2.1 Materials

The starting materials for the analysis include analytical-grade ZnO (purity >99 %, Sigma-Aldrich, India), MnO_2 (purity >99 %, Sigma-Aldrich, India), and $BaCO_3$ (purity >99.5 %, Sigma-Aldrich, India). ZnO was employed as the main matrix material; MnO_2 was used as a nonlinear electrical modifier, while $BaCO_3$ was utilized as a doping material (precursor for BaO). All powders were used as supplied, without additional purification procedures. According to the manufacturer's specifications, the average particle sizes of the ZnO and MnO_2 powders are around 2 µm.

2.2 Synthesis of ZnO–MnO_2 Ceramic Varistors

The three compositions considered had 0 wt.% (undoped, called ZMB0), 0.05 wt.% (called ZMB0.05), and 0.10 wt.% (called ZMB0.10) BaO concentrations, corresponding to the amount of $BaCO_3$ used. The base composition for all samples was held constant at 99.95 mol% ZnO and 0.05 mol% MnO_2 (refer to Table 2). The powders were weighed carefully with an analytical balance to an accuracy of ±0.0001 g, then suspended in isopropyl alcohol (IPA) as the milling medium. The resulting slurry was dried in a convection oven at 60 °C for 12 h, then passed through a 100 µm stainless steel sieve to break agglomerates.

Table 2. Investigated systems (nominal compositions)

A. System	B. ZnO (mol%)	C. MnO_2 (mol%)	D. BaO (mol%)	E. BaO (wt.%)
F. ZMB_0	G. 99.95	H. 0.05	I. 0.00	J. 0.00
K. $ZMB_{0.05}$	L. 99.90	M. 0.05	N. 0.05	O. 0.05
P. $ZMB_{0.10}$	Q. 99.85	R. 0.05	S. 0.10	T. 0.10

Green compacts (10 mm diameter, about 2 mm thickness) were prepared by uniaxial pre-pressing at 50 MPa followed by cold isostatic pressing at 200 MPa. For each composition and sintering temperature, 15 specimens were prepared (total n = 3 compositions × 4 temperatures × 15 specimens = 180). Sintering was carried out in a box furnace (Nabertherm, Germany) in air at 1050, 1100, 1150, and 1200 °C. The heating and cooling rates were both set at 3 °C min^{-1}. The dwell time at the peak temperature was 2 h for all samples. After sintering, samples were polished to remove surface layers and cleaned ultrasonically in ethanol.

2.3 Characterization Methods

Phase identification was performed using X-ray diffraction (XRD) with a Philips X'Pert diffractometer employing Cu Kα radiation (λ = 1.54184 Å) operated at 40 kV and 40 mA. Diffraction data were collected over a 2θ range of 10°–90° using a step size of 0.02° and a scanning rate of 2° min^{-1}. The average crystallite size (D) was estimated using the Scherrer equation (Eq. 1):

$$D = \frac{K\lambda}{\beta \cos\theta} \quad (1)$$

where K is the shape factor (0.94), λ is the X-ray wavelength (1.54184 Å), β is the full width at half maximum (FWHM) of the diffraction peak expressed in radians, and θ is the Bragg diffraction angle. The lattice microstrain (ε) was determined using the Williamson–Hall method, while the dislocation density (δ) was estimated using Eq. (2):

$$\delta = \frac{1}{D^2} \quad (2)$$

These parameters were used to evaluate the influence of BaO addition on the crystallographic characteristics and defect structure of the ZnO–MnO_2 varistor ceramics.

Microstructure and elemental composition analysis were carried out via Scanning Electron Microscope (SEM) equipped with Energy Dispersive X-ray Spectroscopy (EDX) using a JEOL JSM 6610LV instrument (acceleration voltage 20 kV, working distance 10 mm). Grain sizes were analyzed from SEM images using ImageJ (version 1.53, National Institutes of Health, USA). In this case, for each test specimen, more than 200 grains were measured from three randomly selected SEM images. Grain size values presented in this study are reported as the arithmetic mean ± standard deviation (SD). Relative density was measured using Archimedes' method, with distilled water as the liquid medium (ASTM B962 17).

Optical measurements were performed using a Shimadzu UV-2600 spectrophotometer with an integrating sphere. Spectra of diffuse reflection were converted to absorption spectra using the Kubelka–Munk transformation. Direct bandgap (Eg) was evaluated based on Tauc's plots $(\alpha h\nu)^2$ vs photon energy (hν), where α is an absorption coefficient.

Electrical properties were studied on samples cut to parallelepiped form (tolerance in thickness ±0.02 mm) and contacted by silver paste electrodes (diameter 6 mm) annealed at 500 °C within 15 min. J-E characteristics were

measured at room temperature (25 ± 2 °C) by means of a Keithley 2410 source meter in conditions of a DC voltage scan (from 0.1 to 10 mA cm^{-2} in steps of 0.1 V). The nonlinear coefficient α was obtained from the relation $\alpha = \log(J_2/J_1)/\log(E_2/E_1)$ for J_1 = 0.1 mA cm^{-2} and J_2 = 1 mA cm^{-2}. The breakdown electric field Eb is equal to the value at which J = 1 mA cm^{-2}. Temperature-dependent J-E measurements (25–150 °C) were made by means of a thermoelectric stage (precision ±0.5 °C). For each composition and sintering temperature, three independently prepared samples were measured; each sample was scanned five times. Reported values are mean ± SD; experimental uncertainty was estimated at ±5 % based on repeated measurements.

3. Results and Discussion

3.1 Particle Size Distribution of Precursor Powders

The particle size distributions of ZMB_0, $ZMB_{0.05}$, and $ZMB_{0.10}$ powder mixtures are depicted in Figure 1. The distribution pattern is observed to be asymmetrical, polymodal, and decreasing. In all cases, the dominant particle sizes fall into the fine-to-medium range. The undoped sample (ZMB0) possesses a D50 value of 2.05 µm. On the other hand, samples doped with BaO show smaller D50 values. These values include 1.51 µm for $ZMB_{0.05}$ and 1.46 µm for $ZMB_{0.10}$. Based on the smaller span values (1.6 for undoped and 1.3 for doped), it can be inferred that BaO doping alters the surface charge properties of the ZnO particles, thereby preventing agglomeration.

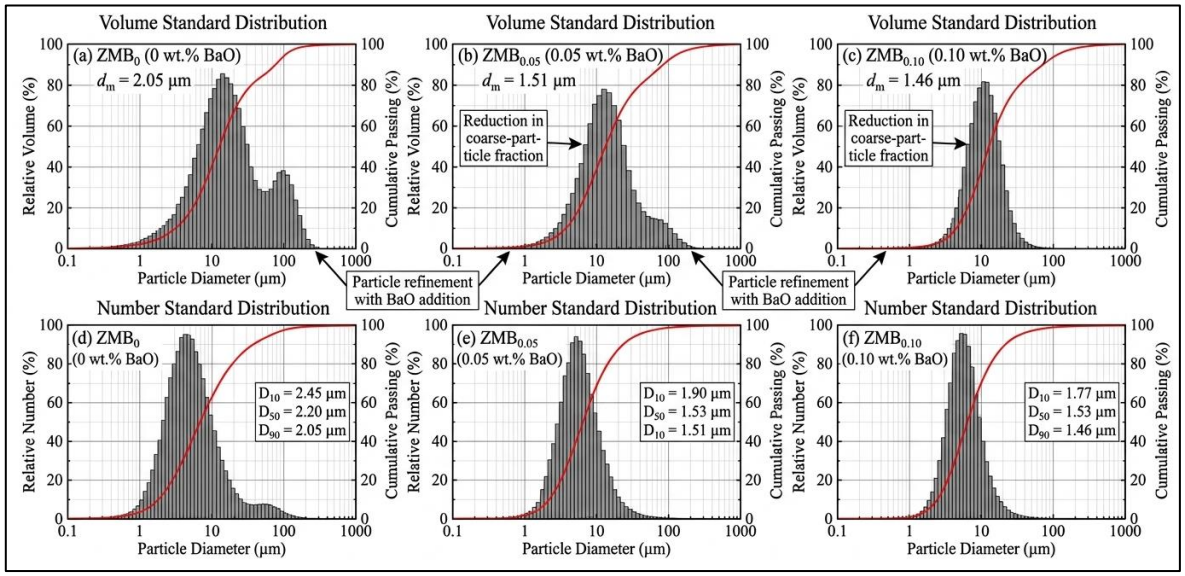

Figure 1. Laser diffraction particle size distributions of ZnO–MnO_2–BaO powders, indicating improved dispersion in BaO-doped samples.

3.2 X-Ray Diffraction Analysis

From the diffractograms of all the samples (Figure 2), it can be seen that the hexagonal wurtzite form of ZnO (ICSD #31052) is the major phase in the samples. However, no diffraction peaks associated with crystalline BaO, $BaCO_3$, and Ba-containing secondary phases have been detected in the X-ray diffraction patterns within the sensitivity range of detection (approximately 2-3 wt.%). Therefore, it can be postulated that Ba is introduced into the ZnO structure in small amounts, forming the amorphous GB phase or precipitated particles. Analysis of the most intense (101) diffraction peak shows that it shifts towards higher 2θ angles with increasing BaO content. For the undoped ZMB0 sample, the (101) diffraction peak is observed at 2θ = 36.25°; for ZMB0.05 and ZMB0.10, these values are 36.31° and 36.29°, respectively. According

to Bragg's equation ($n\lambda = 2d \sin\theta$), the higher angle indicates a decrease in interplanar distance (d). At the same time, considering the ionic radii of Ba^{2+} ions (1.35 Å, CN = 6) being larger than that of Zn^{2+} ions (0.74 Å, CN = 4), such a result appears to be surprising. Three potential mechanisms include: Ba^{2+} occupying interstitial sites, causing lattice strain without any substitution; segregation of Ba^{2+} to the grain boundaries, leading to lattice distortion in the neighboring grains; and formation of Ba^{2+} defects such as Ba^{2+}–VZn, which causes contraction of the lattice structure.

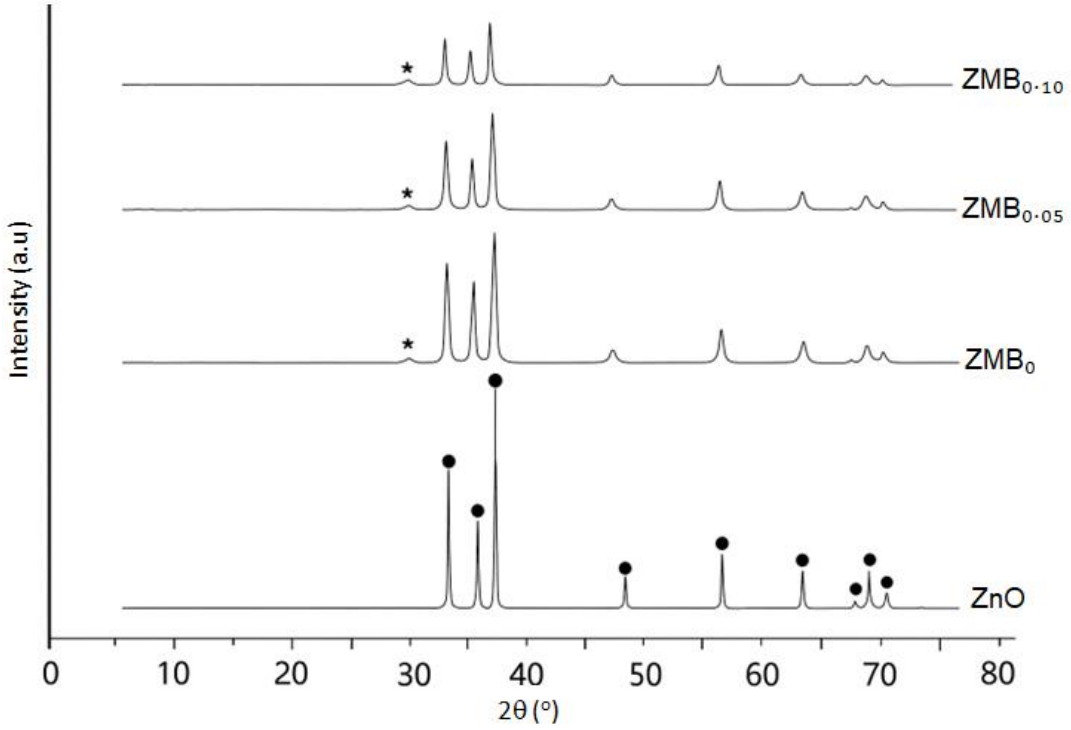

Figure 2. XRD patterns of BaO-doped ZnO–MnO_2 varistors sintered at 1200 °C, showing wurtzite ZnO as the primary phase. Inset: (101) peak shift with BaO addition.

Table 3 provides details of the structural parameters obtained from XRD studies. Crystallite sizes calculated via the Scherrer equation show that D has been refined from 12.56 ± 2.31 nm (ZMB0) to 10.47 ± 1.20 nm (ZMB0.05) and 10.48 ± 1.67 nm (ZMB0.10). These results clearly show that the addition of BaO segregates, pinning grain boundary migration, and hence limiting the crystallite size in sintered samples. Microstrain and dislocation densities have both increased after BaO segregation, consistent with the observed lattice distortion. The MnO_2 does not appear as a distinct phase due to its good solid solubility within the ZnO structure, consistent with Hume-Rothery's rules [34] as their ionic radii are similar (Mn^{4+} 0.53 Å and Zn^{2+}).

Table 3. Structural parameters derived from XRD for ZMB samples

Sample	2θ (101) (°)	Lattice a (Å)	Lattice c (Å)	c/a ratio	Crystallite size D (nm)	Microstrain ε ($\times10^{-3}$)	Dislocation density δ ($\times10^{15}$ m^{-2})
ZMB_0	36.25 ± 0.02	3.249 ± 0.001	5.207 ± 0.002	1.603	12.56 ± 2.31	1.12 ± 0.08	6.34 ± 0.42
$ZMB_{0.05}$	36.31 ± 0.02	3.245 ± 0.001	5.201 ± 0.002	1.603	10.47 ± 1.20	1.35 ± 0.10	9.12 ± 0.65
$ZMB_{0.10}$	36.29 ± 0.02	3.246 ± 0.001	5.203 ± 0.002	1.603	10.48 ± 1.67	1.34 ± 0.09	9.10 ± 0.58

3.3 UV-Visible Optical Properties

Figure 3 shows the Tauc plot of ZMB samples with BaO content of 0.00 %, 0.05 %, and 0.10 %, showing their optical absorption behavior and band gaps, respectively. The pure ZMB0 sample shows a direct band gap of 3.34 ± 0.03 eV, in agreement with reported values for pure ZnO (3.30–3.37 eV). Doping with BaO lowers the band gap to 2.79 ± 0.02 eV and 2.80 ± 0.02 eV, respectively, for ZMB0.05 and ZMB0.10. The optical properties are summarized in Table 4. The decrease in band gap (ΔEg ≈ 0.55 eV) can be accounted for in terms of higher structural disorder and lattice strain (ε increased from 1.12 to 1.35 × 10^{-3}) leading to band tail states; generation of defect states within the band gap by the introduction of Ba^{2+}; and possibly quantum confinement effect due to lower crystallite sizes (12.6 nm → 10.5 nm). The higher Urbach energy (Eu) of about 140 meV, compared to 85 meV, supports the formation of band-tail states [36,37]. The substantial bandgap reduction is likely associated with defect-related localized states and increased structural disorder rather than with direct band-structure modification.

Table 4. Optical properties of BaO-doped ZnO–MnO_2 varistors

Sample	**Direct bandgap Eg (eV)**	**Urbach energy Eu (meV)**	**Crystallite size D (nm)**	**Peak absorption λ_{max} (nm)**
ZMB_0	3.34 ± 0.03	85 ± 5	12.56	371
$ZMB_{0.05}$	2.79 ± 0.02	142 ± 8	10.47	444
$ZMB_{0.10}$	2.80 ± 0.02	140 ± 7	10.48	443

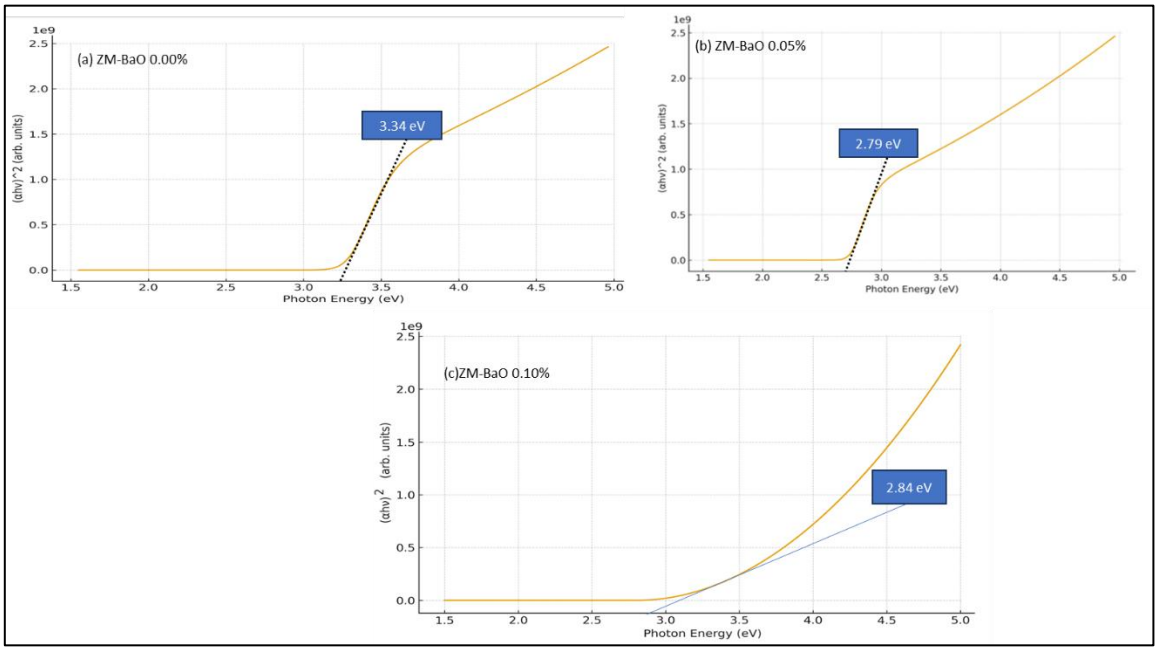

Figure 3. Tauc plots of ZM–BaO samples: (a) ZMB_0, (b) $ZMB_{0.05}$, and (c) $ZMB_{0.10}$, showing bandgap narrowing with BaO addition.

3.4 Sintering Behavior and Densification

Figure 4a and 4b show the linear shrinkage and shrinkage rate curves of the BaO-doped ZnO–MnO_2 composites measured up to 1300 °C. The shrinkage occurs in three distinct stages. Stage I (25–800 °C) exhibits shrinkage below 2 %, corresponding to initial particle rearrangement, removal of organic binders, and decomposition of $BaCO_3$ (which decomposes to BaO and CO_2 above about 800 °C). Stage II (800–1000 °C) is characterized by a sharp increase in shrinkage rate with a maximum at about 910 °C. The rapid densification observed between 800 and 1000 °C may indicate liquid-phase-assisted sintering; however, direct evidence of transient liquid formation was not obtained in the present study. Stage III (1000–1200 °C) shows a decreasing shrinkage rate as pore closure nears completion. Table 5 presents the densification parameters for samples sintered at 1200 °C. All samples achieved relative densities above 95 %, confirming the effectiveness of BaO as a densification aid. The slight decrease in density for $ZMB_{0.10}$ at 1200 °C may be due to exaggerated grain growth and pore entrapment (see Section 3.5).

Table 5. Densification parameters of BaO-doped ZnO–MnO_2 varistors sintered at 1200 °C

Parameter	ZMB_0	$ZMB_{0.05}$	$ZMB_{0.10}$
Relative density (%)	95.5 ± 0.5	95.9 ± 0.4	95.7 ± 0.5
Linear shrinkage (%)	17.6 ± 0.3	18.2 ± 0.3	18.8 ± 0.4
Apparent density (g cm^{-3})	5.52 ± 0.03	5.54 ± 0.03	5.53 ± 0.03

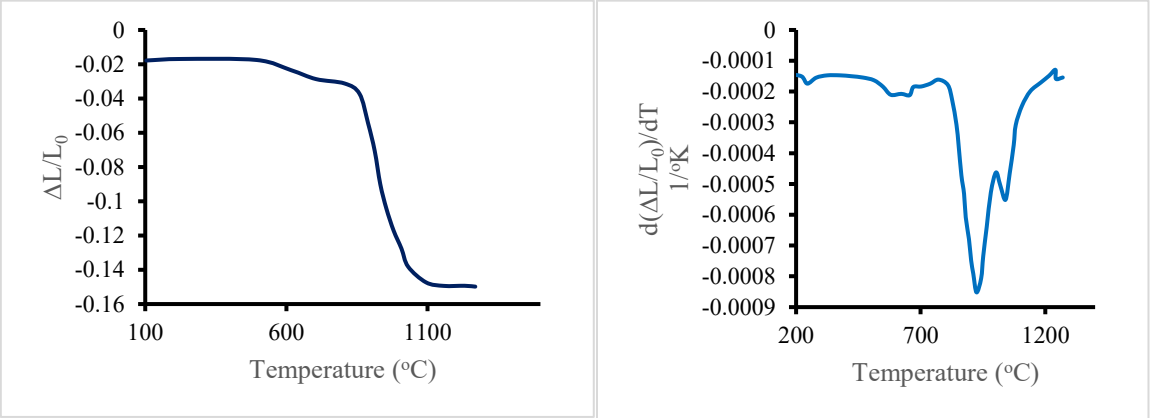

Figure 4. Sintering behavior of BaO-doped ZnO–MnO_2 composites: (a) linear shrinkage and (b) shrinkage rate versus temperature, showing three sintering stages.

3.5 Microstructural Evolution

Figure 5 presents SEM micrographs of $ZMB_{0.10}$ composite sintered at (a) 1050 °C, (b) 1150 °C, and (c) 1200 °C. The microstructure shows homogeneous grain morphology with clearly defined grain boundaries. BaO doping promotes grain growth with increasing sintering temperature. Table 6 summarises the average grain sizes for all compositions and sintering temperatures. The grain growth follows a classical kinetic law, with BaO lowering the activation energy for grain boundary migration. The homogeneous grain structure at 1150 °C for $ZMB_{0.10}$ suggests an optimal dopant level for uniform grain boundary wetting. EDX analysis (Figure 6, Table 7) confirms the segregation of Ba at grain boundaries. Local grain boundary composition from point EDX analysis shows Ba enrichment of approximately 5–10 at.% at boundaries, compared to less than 1 at.% in the bulk grain interiors, yielding an enrichment factor of about 8.

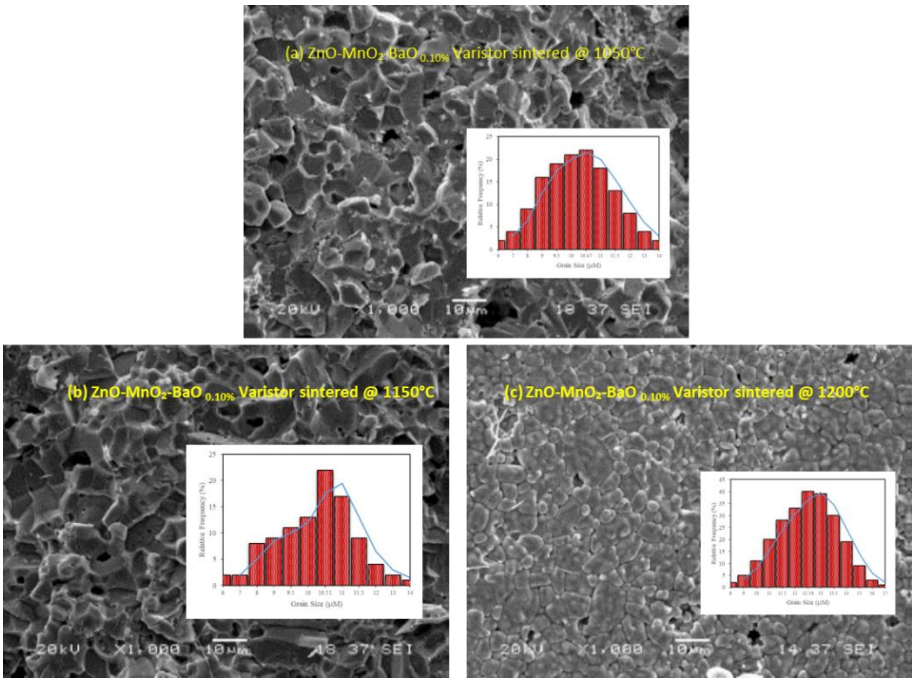

Figure 5. SEM micrographs (5000×) of $ZMB_{0.10}$ sintered at (a) 1050 °C, (b) 1150 °C, and (c) 1200 °C, showing grain growth and well-defined grain boundaries.

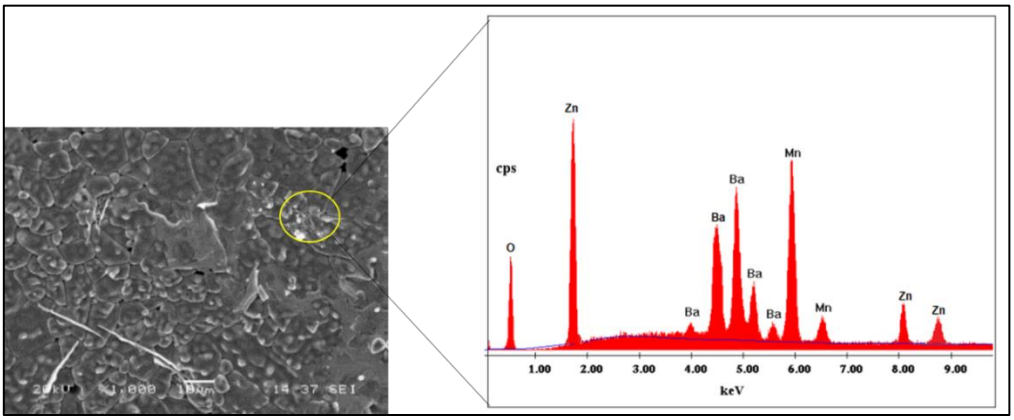

Figure 6. SEM–EDX evidence of grain-boundary Ba segregation in $ZMB_{0.10}$.

Table 6. Average grain size (μm, mean ± SD, n ≥ 200 grains) of ZMB varistors

Sintering Temperature (°C)	ZMB_0	$ZMB_{0.05}$	$ZMB_{0.10}$
1050	12 ± 1	12 ± 1	14 ± 1
1100	20 ± 1	22 ± 1	24 ± 1
1150	30 ± 2	32 ± 2	34 ± 2
1200	38 ± 2	40 ± 2	42 ± 2

Table 7. Local grain-boundary composition from point EDX analysis ($ZMB_{0.10}$ sintered at 1200 °C)

Element	Grain boundary (at.%)	Grain interior (at.%)	Enrichment factor
O Kα	10–15	12–16	~1
Zn Kα,Kβ; Lα,Lβ	70–80	80–85	~0.9
Mn Kα,Kβ	4–8	2–5	~1.8
Ba Lα,Lβ,Lγ	5–10	<1	>8

3.6 Electrical Performance and Grain Boundary Physics

Figure 7 presents the current density–electric field (J–E) characteristics of the ZMB varistors sintered at different temperatures, while the corresponding electrical parameters are summarized in Table 8. An increase in the nonlinear coefficient (α) was observed with increasing BaO concentration and sintering temperature. The value of α increased from 7 for the undoped composition to 9 for the sample containing 0.10 wt.% BaO sintered at 1200 °C, indicating an improvement in the grain-boundary barrier characteristics. Simultaneously, the breakdown field (E_b) decreased with increasing sintering temperature and BaO content. This behavior is primarily associated with grain growth during sintering. For a specimen of constant thickness (t), the number of electrically active grain boundaries (N) is inversely proportional to the average grain size (d) and can be expressed as Eq. (3):

$$N = \frac{t}{d} \quad (3)$$

The overall breakdown voltage (V_b) is determined by the cumulative voltage drop across individual grain boundaries (V_{GB}) and is given by Eq. (4):

$$V_b = NV_{GB} \quad (4)$$

Substituting Eq. (3) into Eq. (4) yields:

$$V_b = \frac{t}{d} V_{GB} \quad (5)$$

Accordingly, the breakdown field is expressed as:

$$E_b = \frac{V_b}{t} = \frac{V_{GB}}{d} \quad (6)$$

This inverse relationship explains the observed reduction in the breakdown field with increasing grain size.

The temperature-dependent J–E characteristics shown in Figure 8 suggest that Schottky thermionic emission is the dominant conduction mechanism in the pre-breakdown region. The current density can be described by the Schottky emission equation:

$$J = A^* T^2 \exp\left[-\frac{q\left(\phi_b - \sqrt{\frac{qE}{4\pi\varepsilon}}\right)}{kT}\right] \quad (7)$$

where $A^*$is the Richardson constant, q is the elementary charge, k is Boltzmann's constant, E is the applied electric field, and $\varepsilon$is the dielectric permittivity. The approximately linear relationship observed in the $\ln(J)$versus $E^{1/2}$plot (Figure 9) supports the applicability of the Schottky emission model. The Schottky barrier height (ϕ_b) obtained from the Arrhenius analysis (Figure 10) was calculated to be 0.98 ± 0.04eV. This value is higher than that commonly reported for conventional Bi_2O_3-based ZnO varistors (approximately 0.8 eV), suggesting that the higher barrier height is consistent with the formation of stronger grain-boundary potential barriers.

Table 8. Electrical properties of ZnO–MnO_2–BaO varistors sintered at different temperatures

Sintering Temp (°C)	Sample	Average grain size (μm)	Nonlinear coefficient α	Breakdown field Eb (V/mm)	Leakage current JL (μA/cm² @ 0.8 Eb)
1050	ZMB_0	12 ± 1	2 ± 0.3	930 ± 46	85 ± 8
	$ZMB_{0.05}$	12 ± 1	3 ± 0.4	890 ± 44	78 ± 7
	$ZMB_{0.10}$	14 ± 1	4 ± 0.4	850 ± 42	70 ± 6
1100	ZMB_0	20 ± 1	4 ± 0.4	520 ± 26	55 ± 5
	$ZMB_{0.05}$	22 ± 1	5 ± 0.5	480 ± 24	48 ± 4
	$ZMB_{0.10}$	24 ± 1	6 ± 0.5	450 ± 22	42 ± 4
1150	ZMB_0	30 ± 2	5 ± 0.5	330 ± 16	40 ± 4
	$ZMB_{0.05}$	32 ± 2	6 ± 0.5	300 ± 15	35 ± 3
	$ZMB_{0.10}$	34 ± 2	7 ± 0.5	280 ± 14	32 ± 3
1200	ZMB_0	38 ± 2	7 ± 0.5	180 ± 9	45 ± 5
	$ZMB_{0.05}$	40 ± 2	8 ± 0.5	160 ± 8	35 ± 4
	$ZMB_{0.10}$	42 ± 2	9 ± 0.5	140 ± 7	28 ± 3

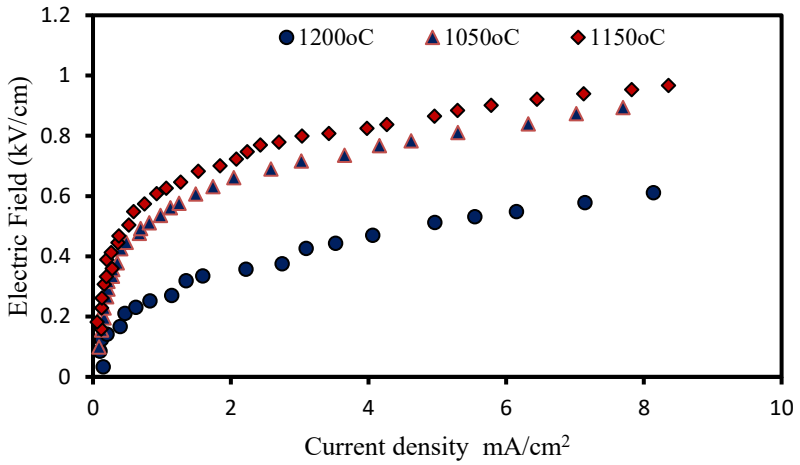

Figure 7. J–E characteristics of ZMB varistors at different sintering temperatures, showing improved nonlinearity with BaO addition.

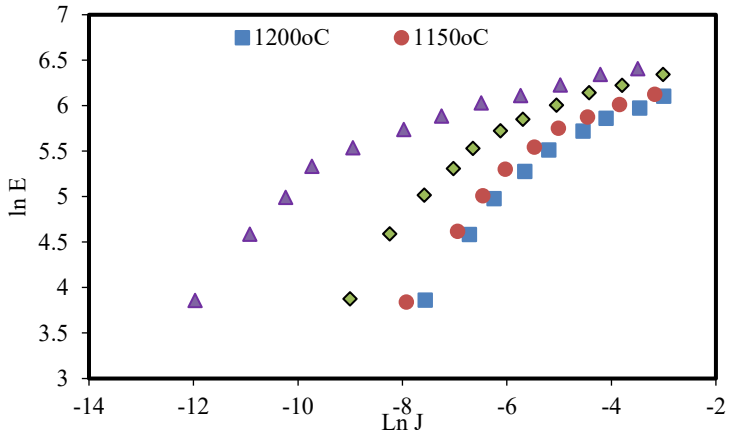

Figure 8. Temperature-dependent J–E behavior of $ZMB_{0.10}$, showing thermionic emission conduction.

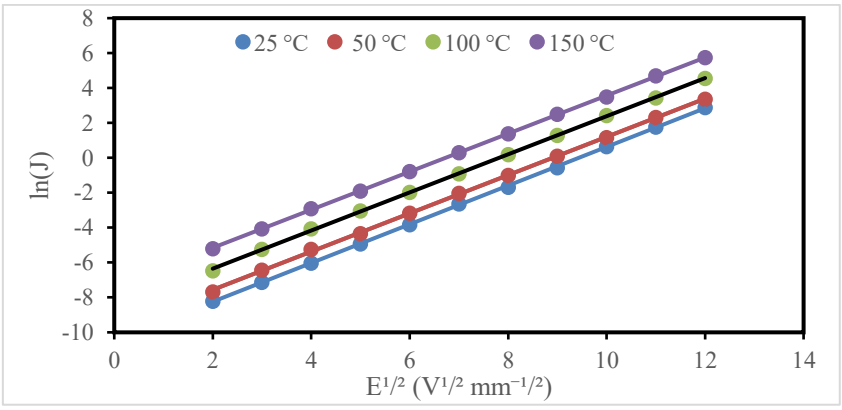

Figure 9. Schottky emission analysis of ZMB0.10: ln(*J*) versus $E^{1/2}$ at different temperatures.

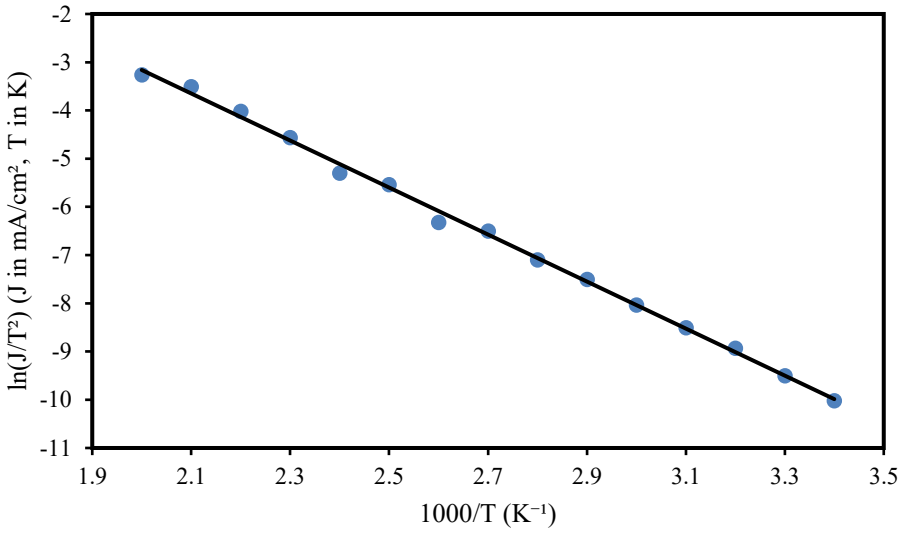

Figure 10. Arrhenius analysis of ZMB0.10 varistor showing a Schottky barrier height of 0.98 ± 0.04 eV.

3.7 Proposed Mechanism for BaO-Induced Grain Boundary Engineering

Based on the combined XRD, SEM/EDX, and electrical data, an evidence-based mechanism is proposed. During liquid-phase-assisted sintering, Ba^{2+} ions, due to their large ionic radius and low solubility in ZnO (less than 0.01 mol% at 1200 °C), are rejected from growing ZnO grains and segregate strongly to grain boundaries and triple points. The segregation enrichment factor of approximately eight at grain boundaries is consistent with literature reports for large cations in ZnO. The isolated Ba^{2+} ions act as electron acceptors, thereby trapping charge carriers and making the interface layer negatively charged. This phenomenon is balanced by the presence of a positively charged depletion layer within the adjacent ZnO grains, resulting in the formation of two Schottky barriers.

Furthermore, due to MnO_2, which increases the number of donor defects, the Schottky barrier height is expected to increase even further. The presence of BaO pins the grain boundary, thereby restricting grain growth. The sintering process was optimally performed between 1150 °C and 1200 °C, with 0.10 wt. added.% BaO ensures that grain growth is optimized, thereby lowering Eb. However, a homogeneous, compact microstructure is still achieved with clean grain boundaries. The high Schottky barrier height (0.98 eV) caused by BaO/MnO_2 segregation results in voltage-dependent varistor behavior. Under low voltages, the barrier stops the flow of charge carriers. As we approach the breakdown voltage, the barrier becomes narrow, allowing easy tunneling.

The comparison of the performances of the current $BaO\text{-}ZnO\text{-}MnO_2$ varistors and recent ZnO varistors is given in Table 9. The current $BaO\text{-}ZnO\text{-}MnO_2$ system shows a very low breakdown field (140 V mm^{-1}) and an average α value (9), similar to other multi-dopants but at a lower cost.

Table 9. Comparison with recent ZnO-based varistor literature (2020–2026)

Reference	System	Sintering Temp (°C)	Grain size (μm)	α	Eb (V/mm)	Key feature
Feng et al. 2022 [11]	NiO–ZnO	1100	9–14	8–12	300–420	High Eb
Cui et al. 2023 [12]	Mn–ZnO (low-temp)	875–1000	5–10	15–20	80–120	Low Eb, complex process
Tian et al. 2022 [13]	Cr_2O_3–ZnO	1150	8–15	10–18	250–400	Moderate performance
Zhang et al. 2021 [14]	Er_2O_3–ZnO	1150	10–20	12–22	200–350	High cost
Fan & Freer 1997 [18]	ZnO–BaO	—	—	5–10	—	No MnO_2, limited data
Liptai et al. 2024 [29]	Recycled ZnO	1100	10–20	8–12	300–500	Sustainability focus
Hassan et al. 2025 [32]	Multi-dopant ZnO	1000–1200	10–25	8–15	200–380	Complex optimisation
Present study	BaO–ZnO–MnO_2	1200	42	9	140	Low Eb, simple composition

4. Conclusions

This work demonstrates the effectiveness of BaO as a grain-boundary engineering material in invaristor ceramics. BaO additions ranging from 0.05 to 0.10 wt.% increase the density of the ceramic materials above 95% when sintered above 1050 °C. Average grain size in 0.10 wt.% BaO doped samples ranges from 14 ± 1 μm at 1050 °C to 42 ± 1 μm at 1200 °C. BaO causes lattice distortion by contracting both the a-axis and c-axis. X-ray diffraction results show that crystallite sizes decrease from 12.6 nm to 10.5 nm due to Ba^{2+} segregation at grain boundaries, without affecting the crystal structure. Energy-dispersive X-ray analysis indicates Ba enrichment in the ceramic materials by about 8. Optical band gap decreases with increasing doping of BaO from 3.34 to 2.79 eV because of the creation of defect states due to the microstrain increase from 1.12 to 1.35×10^{-3}. Electrical properties of the ceramic materials sintered at 1200 °C with 0.10 wt% BaO are α = 9 and Eb = 140 V mm^{-1}. With a value of 0.98 eV, the Schottky barrier is higher than the typical values for Bi_2O_3-based systems (0.70–0.85 eV). This suggests that grain boundary potentials are relatively strong. A lower value of Eb obeys the conventional relation with the grain size, as the exponent is equal to one ($Eb \propto 1/d$, $R^2 = 0.97$). Thus, BaO can be regarded as a powerful dopant at a very low concentration of 0.10 wt.% for zinc oxide-manganese dioxide varistors. Such a compound can serve as a less expensive alternative to rare-earth dopants. With a low

breakdown field (140 V mm^{-1}) and a nonlinearity factor α = 9, it can be used in low-voltage applications in consumer goods, automobiles, and low-voltage power sources, etc. Future experiments should include direct measurement of interface states using the DLTS method, evaluation of their stability through long-term DC aging studies, optimization of a multi-doping regime, and TEM analysis of their effects

Acknowledgments

The author gratefully acknowledges the support of the Ministry of Education, Iraq, and Geniuses High School for Outstanding Students, under the General Directorate of Al-Rusafa the Third, Baghdad, Iraq, for providing the institutional support and facilities necessary to carry out this research.

Conflict of Interest

The authors declare no conflict of interest.

References

[1]. Lao X, Ren X, Yan Y, et al. (2022) Effects of dispersant on electrical properties of zinc-oxide varistors and methods to improve protection performance. *J Electron Mater* 51: 5169–5180.

[2]. Tian J, Wu Y, Tian H, Xu Y, Zhao J, Lu P, Zhang B, Wang G (2023) Microstructure and nonlinear electrical properties in Na_2CO_3–ZnO varistor ceramics. *Mater Sci Eng B* 300: 117084.

[3]. Bouchekhlal A, Boulesbaa M (2022) Synthesis and characterization of ZnO-based varistor ceramics: Effect of sintering temperatures. *Microelectron Int* 39: 110–120.

[4]. Ivetic T, Nikolic M, Slankamenac M, Zivanov M, Minic D, Nikolic P, Ristic M (2007) Influence of Bi_2O_3 on microstructure and electrical properties of ZnO–SnO_2 ceramics. *Sci Sinter* 39: 229–240.

[5]. Chen R, Li Q, Yu X, Chen L, Li H (2019) Approaching practically accessible solid-state batteries: Stability issues related to solid electrolytes and interfaces. *Chem Rev* 120: 6820–6877.

[6]. Tian T, Zheng L, Bernik S, Man Z, Shi X, Ruan X, Li G (2022) Influence of Cr_2O_3 doping on the electrical characteristics of novel ZnO–Cr_2O_3-based varistor ceramics. *Mater Res Bull* 159: 112111.

[7]. Saji VS (2023) Corrosion and materials degradation in electrochemical energy storage and conversion devices. *ChemElectroChem* 10: e202300136.

[8]. Thy LTM, Thanh LNP, Dat NT, Dat NM (2025) Review on the application of inorganic UV filters in sunscreens: Mechanisms, evaluation methods, toxicity, and safety enhancements. *Results Surf Interfaces* 20: 100580.

[9]. Matsuoka M (1971) Nonohmic properties of zinc oxide ceramics. *Jpn J Appl Phys* 10: 736–746.

[10]. Cao W, Xie X, Wang Y, Chen M, Qiao Y, Wang P, Zhang Y, Liu J (2019) Effect of Pr_6O_{11} doping on the microstructure and electrical properties of ZnO varistors. *Ceram Int* 45: 24777–24785.

[11]. Feng Y, Li Y, Zhao X, Zhao X, Guo M, Yang L, Liao R (2022) Effect of DC ageing on NiO-doped ZnO varistor ceramics. *J Mater Sci Mater Electron* 33: 1–11.

[12]. Cui W, Zhao M, Chen M, Liu Z, Chen H, Deng L (2023) Effect of Mn on ZnBiMnO varistor ceramics sintered at 875 °C. *Ceram Int* 50: 7597–7604.

[13]. Tian T, Zheng L, Bernik S, Man Z, Shi X, Ruan X, Li G (2022) Influence of Cr_2O_3 doping on ZnO-based varistor ceramics. *Mater Res Bull* 159: 112111.

[14]. Zhang L, Liu W, Gao J, Kong F, Li Y, Li S (2021) Effects of Er_2O_3 doping on microstructure and electrical properties of ZnO–Bi_2O_3 varistor ceramics. *Ceram Int* 47: 32349–32358.

[15]. Meng P, Gu S, Wang J, Hu J, He J (2018) Improving electrical properties of ZnO varistors by indium and gallium doping. *Ceram Int* 44: 1168–1175.

[16]. Cui B, Niu J, Peng P, Shi L, Du S, Liu J, Xu D (2020) Flash sintering and electrical properties of ZnO–Bi_2O_3–M varistor ceramics. *Ceram Int* 46: 14913–14920.

[17]. Xu M, Cai C, Shi Y, Xie M, Wu Y, Liu Y, Peng J, Bao J, An S (2022) Grain growth control of ZnO–V_2O_5-based varistors by $PrMnO_3$ addition. *Micromachines* 13: 214.

[18]. Fan J, Freer R (1997) Varistor properties of ZnO–BaO ceramics. *J Mater Sci* 32: 415–419.
[19]. Lungu MV (2023) Effects of dopants and processing parameters on ZnO–V_2O_5-based varistors: A review. *Materials* 16: 3725.
[20]. Xie P, Wang Z, Wu K (2022) Evolution of electron traps at grain boundaries in ZnO varistor ceramics. *Materials* 15: 1098.
[21]. Song L, Fu Z, Ye Z, He J (2025) Microstructure evolution in nano ZnO@SiO_2 core–shell powders. *Ceram Int* 51: 50324–50335.
[22]. Chen B, Wang B, Gao P, Zhang P, Chen H (2021) Effects of particle size and annealing on ZnO varistors. *J Alloys Compd* 872: 159638.
[23]. Liang J, Zhao X, Sun J, Ren L, Liao R, Yang L, Li W (2020) Enhanced electrical properties of ZnO varistors by spark plasma sintering. *Ceram Int* 46: 15076–15084.
[24]. Gunnewiek RFK, Perdomo CPF, Cancellieri IC, Cardoso ALF, Kiminami RHGA (2020) Microwave sintering of nanostructured ZnO-based varistors. *Ceram Int* 46: 15044–15052.
[25]. Fu Z, He J, Lu J, Fang Z, Wang B (2019) Dielectric relaxation and degradation of ZnO varistors. *Ceram Int* 45: 21900–21907.
[26]. Cui F, Xu Z, Chu R, He X, Guo X, Li G (2021) Low-temperature sintering of ZnO–Bi_2O_3 varistor ceramics. *Ceram Int* 47: 4118–4126.
[27]. Li J, Yang S, Pu Y, Zhu D (2021) Effects of pre-calcination and sintering temperature on ZnO varistors. *Mater Sci Semicond Process* 123: 105529.
[28]. Sendi RK, Ali AM (2021) Effect of cooling rate on nonlinear stability of ZnO-based varistors. *Microsc Res Tech* 84: 723–732.
[29]. Liptai P, Nagy Š, Dolník B, Matvija M, Pirošková J (2024) Optimization of recycled ZnO-based varistor manufacturing. *Heliyon* 10: e35898.
[30]. Han J, Senos AMR, Mantas PQ (2002) Varistor behaviour of Mn-doped ZnO ceramics. *J Eur Ceram Soc* 22: 1653–1660.
[31]. Cao W, Guo Y, Su J, et al. (2023) Effect of sintering temperature on ZnO varistors. *J Electron Mater* 52: 1266–1273.
[32]. Hassan M, Hussain M, Ali M, et al. (2025) Influence of processing parameters on ZnO-based varistors. *Discover Electron* 2: 21.
[33]. Kobayashi R, Kishi T, Katayanagi Y, Yano T, Matsushita N (2018) Fabrication of nitrogen-doped ZnO nanorods. *RSC Adv* 8: 23599–23605.
[34]. Martin A, Thuo M (2023) Beyond Hume–Rothery rules. *Acc Mater Res* 4: 809–813.
[35]. Pillai SC, Kelly JM, Ramesh R, McCormack DE (2013) Advances in synthesis of ZnO nanomaterials for varistors. *J Mater Chem C* 1: 3268–3281.
[36]. Das B, Aguilera I, Rau U, Kirchartz T (2022) Effect of doping on perovskite solar cells. *Adv Opt Mater* 10: 2101947.
[37]. Markevich I, Stara T, Vorona I, Isaieva O, Gule Y, Melnichuk O , Khomenkova L (2023) Role of $ZnMn_2O_4$ phase in ZnO:Mn varistors. *Semicond Phys Quantum Electron Optoelectron* 26: 255–259.